

A Survey of Chemical Nonequilibrium in Argon Arc Plasma

Margarita Baeva¹

Received: 30 October 2016 / Accepted: 8 December 2016 / Published online: 18 December 2016
© Springer Science+Business Media New York 2016

Abstract The widespread application of electric arcs is closely related to the continuous research interest over the course of many years. The present survey is concerned with chemical and excitation nonequilibrium in atmospheric pressure argon plasma generated between a sharpened tungsten cathode and a flat copper anode at current levels of 35–200 A. Advanced fully nonequilibrium modelling is applied to simulate the combination of the wall-confined arc plasma column and the open region in front of the anode in a self-consistent manner in order to pay tribute to the tremendous research work that E. Pfender has done. The new modelling results are presented along with experimental and modelling results of the studies of E. Pfender and his group and other works of relevance.

Keywords Arc plasma · Thermal plasma · Ionization nonequilibrium · Chemical nonequilibrium · Modelling

Introduction

Thermal plasmas generated by electric arcs at atmospheric pressure find widespread applications for plasma processing. They are characterized by temperatures of electrons and heavy particles (atoms and ions) so close to each other that the assumption of local thermodynamic equilibrium (LTE) is often used for their description. According to this assumption, the thermodynamic state of the plasma and its chemical reactivity can be specified by one temperature and pressure only. Based on the assumption of LTE, the majority of diagnostic techniques for thermal plasma have been developed and the transport properties of ionized gases at atmospheric pressure have been found over wide range of temperatures [1–3]. Thereby, wall-confined arc plasmas have been extensively

✉ Margarita Baeva
baeva@inp-greifswald.de

¹ Leibniz Institute for Plasma Science and Technology, INP Greifswald e.V., Felix-Hausdorff-Str. 2, 17489 Greifswald, Germany

studied, in which a DC discharge is ignited in a water-cooled cylindrical tube consisted of stacked copper disks with inner radius of 5 mm [1] and a length significantly larger than the radius. Between and sufficiently far away from the electrodes, the axial gradients in the plasma temperature and in the axial electric field are negligible. The measured values are insensitive to the small pressure drop so that the plasma properties (e.g. electrical and thermal conductivity, the volumetric radiation source) are functions of the radial position only.

However, deviations from LTE in thermal plasma are rather common close to the confining walls, in the near-electrode regions, and the arc fringes of free-burning arcs [4–19]. Departure from equilibrium can occur in various forms. At low arc currents (e.g. 7–15 A [19], 35 A [4], 40–60 A [12] at pressure of 1 atm), electron temperatures substantially exceeding the heavy-particle temperatures and overpopulation of the ground state of argon atoms in comparison to the equilibrium one have been reported. At high arc currents, strong macroscopic flows are induced by the arc itself, in particular by variations of the current-carrying cross-section of the arc (Maecker effect). Effects of chemical nonequilibrium have been related to diffusive and convective transport, and radiation escape [20]. A prominent absorption observed at the line centre of e.g. Ar I 763.5 nm [21], 104.8 nm [13] has been ascribed [22] to non-LTE conditions in the arc fringes where the population of the excited levels differed by many orders of magnitude from values derived under LTE conditions. The temperature distribution obtained by means of spectroscopic measurements [22] showed discrepancy in the vicinity of the cathode in comparison with simulation results based on LTE [23]. Increasing underpopulation of excited Ar I states toward the cathode has been experimentally proven at low arc currents (7–15 A) by means of a spatially resolved relaxation method [17, 18].

Many previous investigations of nonequilibrium argon arcs have dealt with a fully developed cylindrical arc column [5, 7, 24, 25], which reduces the problem to one-dimensional. Other works have been focused on the anode contraction region of the arc [26–31] applying radial profiles of the gas flow and the plasma properties obtained in the one-dimensional model of the arc column. Besides the spatial characterization of the arc plasma, the models differ in their physical description. The most important difference is the treatment of diffusion. While some two-dimensional models [27] assume chemical equilibrium and thermal nonequilibrium and diffusion is ignored, one-dimensional models make use of ambipolar diffusion coefficient due to the negligible radial current component [5, 25]. More recent models [29, 30] of the anode region of the constrictor arc account for diffusive effects caused by gradients in the electron temperature and pressure.

The present work is concerned with the nonequilibrium behaviour of the confined arc and its near-anode region in argon at atmospheric pressure by means of advanced fully nonequilibrium model [31] both at low (down to 35 A) and at high (up to 200 A) arc current levels. It is aimed at paying a tribute to the works of E. Pfender and co-workers over the course of many years which helped to improve especially the understanding of the interaction of the arc with the anode. The near-cathode region has been discussed in previous works [20, 31]. The model unifies the arc and the electrodes in a self-consistent manner and applies a general diffusion representation of the particle fluxes in the arc plasma. The plasma constituents are electrons, atoms and singly charged ions of argon at atmospheric pressure. The solution of the arc model is used as input to a collisional-radiative model to obtain the densities of excited atomic states. The modelling results are presented in comparison with results concerning the wall-stabilized argon arc plasma column and anode region accumulated over the course of many years. The paper is organized as follows: the main features of the advanced fully nonequilibrium model and

the collisional-radiative model are given in “General Features of the Modelling Approaches” section. Results are presented in “Results and Discussion” section. Evidence of chemical nonequilibrium in the wall-confined arc column are considered in “The Cylindrical Column of the Wall-Stabilized Arc Plasma” section. “The Anode Region” section is concerned with the effects occurring in the anode region of the constrictor. Concluding remarks are made in “Concluding Remarks” section.

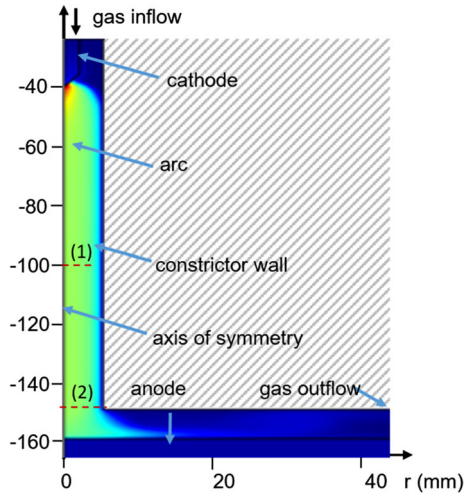
General Features of the Modelling Approaches

Nonequilibrium modelling of an electric arc in its full complexity comprises many aspects. Description of the gas flow, the heat transfer in the plasma and the electrodes, the electric and the magnetic fields, and the plasma chemistry is important to the predictive capability of the model. The plasma chemistry itself represents an extensive field since it includes not only the production of charged particles but also the population of excited states. The latter is essential for the evaluation of emission spectra, determination of electron temperature from the ratio of line intensities as well as for the spectroscopic validation of plasma models. Under a wide range of conditions, the total particle density of excited states is much less compared with the ground state and the electron number density. The ground and the continuum states can be considered as particle pools and the particle flow between them goes through the excited states. Since the relaxation times of the excited states are much shorter in comparison with the relaxation time of the ground state of atoms and ions, the plasma chemistry can be split in a way that the arc model accounts for simplified plasma chemistry concerning the production of charged particles in reactions on ionization and recombination while the atomic state distribution is consequently found by means of a collisional-radiative model with the plasma parameters (electron temperature and density, density of ground state atoms) obtained with the arc model. Following this concept, we present below the general features of the arc and the collisional–radiative model applied in this work.

Model of the Arc

The arc is assumed to obey axial symmetry so that the half of the arc geometry which can be considered as shown schematically in Fig. 1. The arc arrangement includes a ceriated tungsten cathode (WC20) with a radius of 2 mm and a truncated conical tip of 60°. Notice that in a series of relevant experimental works in the past, which will be recalled for comparison below, the cathode was made of thoriated tungsten with thermionic properties similar to that of WC20. The anode is a plate made of copper and is perpendicular to the arc axis. The computational domain contains the arc region and the electrodes with approximately 90,000 mesh elements resulting in 10^6 degrees of freedom solved for. The arc is constricted in a tube with inner radius of 5 mm. The axial distance between the cathode tip and the end of the constrictor tube is 120 mm. The gap between the constrictor and the anode is 10 mm. The arc is operated in argon at atmospheric pressure with arc current in the range 35–200 A and gas flow rate $0.04\text{--}0.135\text{ g s}^{-1}$. This arc geometry and operating conditions allow us to study with one and the same model physical model both the long arc column and the electrode regions, in particular the anode region, and to refer the results to experimental and modelling findings reported over the years.

Fig. 1 Schematic of the arc geometry



A detailed description of the fully nonequilibrium model of the arc and the electrodes is given in a previous publication [31]. Here a summary will be given outlining its main features.

The arc plasma is assumed to be quasi-neutral and to contain electrons, atoms and singly charged ions of argon. A fluid description of the plasma is governed by the Navier–Stokes equation for conservation of mass, momentum and energy. The model forgoes assumptions of thermal and chemical equilibrium. Separate energy equations for electrons and heavy particles are solved. They consider the convective transport of energy, the energy flux due to thermal conduction, transport of enthalpy by diffusive fluxes, and thermal diffusion, and gain/loss of energy due to the electromagnetic field, elastic and inelastic collisions, and radiation. The electrons are characterized by a Maxwellian energy distribution function with a temperature T_e whereas the heavy species (atoms and ions) are assumed to have a common temperature T ($T_e \neq T$). A continuity equation for the ions accounts for diffusion and convection processes and reactions of ionization and recombination. The atom density is obtained from the equation of state and Dalton’s law. The mass (and particle) fluxes of the species are expressed in terms of multicomponent diffusion according to the Stefan–Maxwell equations and the effective binary approach [32, 33]. The diffusive flux for a given species contains volumetric driving forces including gradients in mass fractions, temperature and pressure, and drift of charged particles in the electric field. This allows us to express the electric current density as a sum of diffusive and drift components and to make use of the generalized Ohm’s law. It is worth noting that in this treatment the ambipolar constraint is included in the formulation of the diffusive mass fluxes and the current conservation so that there is no need to calculate an ambipolar diffusion coefficient [34]. Ampère’s law for the self-induced magnetic field is employed to obtain terms appearing in the equation of conservation of momentum (Lorentz force) and energy (Joule heating). The plasma chemistry is simplified and considers production and loss of electrons in electron–atom collisions and recombination according to the concept of prompt ionization and bottleneck in $4s$ levels of argon [5, 35–37]. Radiation losses are considered as a volumetric loss term in the energy equation of electrons [38–41]. Current and heat conduction are considered in the electrodes excluding effects of deterioration (melting, evaporation, erosion) with temperature dependent thermal conductivity and the electrical

conductivity of the solid. The transport parameters in the plasma are calculated following the Chapman–Enskog theory with high order of approximation [42].

The model is completed by appropriate boundary conditions [31, 43]. On the axis of symmetry, all dependent variables have zero gradient. The temperature of heavy particles approaches the surface temperature of the walls. The temperature at the constrictor wall and the opening for gas inflow is set to 300 K while at the base of the cathode it is 500 K. At the bottom of the anode, the heat flux coefficient to the surroundings is set to $50 \text{ W m}^{-2} \text{ K}^{-1}$, corresponding to unforced air cooling. Zero gradient is assumed for the electron temperature on the constrictor wall and the inflow and outflow openings. The outer boundaries are electrically and magnetically insulated except the cathode base and the anode bottom on which electric potential is specified (the anode is grounded). Since the model accounts for thermal and ionization nonequilibrium of the quasi-neutral plasma, the arc core with conditions close to LTE and the pre-sheaths (ionization layers) are unified in the description of the arc plasma. The tiny regions of the space-charge sheaths (thickness of the order of the Debye length) between the bulk plasma and the electrodes are treated as dimensionless. Employing a balance of the electron and the total energy in the space-charge sheath, boundary conditions for the electron temperature and the heat balance of the electrodes have been formulated in [43] and are applied in the present model to couple the quasi-neutral plasma and the electrodes. Contributions of ions and electrons from the bulk plasma and electrons emitted from the metal electrode are taken into account. The normal component of the electron energy flux from the quasi-neutral plasma equals the sum of the energy flux of emitted electrons from the cathode to the sheath and the work of the electric field over the electrons in the sheath. The heat flux to the electrodes includes contributions of heavy particles and electrons and accounts for the power deposited in the sheath and the cooling due to the transit of electrons from the metal into the plasma, power released at the surface due to ion recombination, and black-body radiation. The arc voltage is the difference of electric potential at the cathode base and the anode. Along the cathode surface the electric potential has a jump due to the voltage drop in the space-charge sheath. An iterative procedure is applied to obtain in a self-consistent manner the sheath voltage and the normal current density along the thermionic cathode for a given arc voltage and total arc current.

Collisional–Radiative Model for the Atomic State Distribution

The atomic state distribution function is related to plasma parameters such as electron temperature, electron density, and density of atoms in the ground state. The distribution of the atoms over the excited states is usually obtained in the framework of collisional-radiative models (e.g. [44–50]). A large number of excited states has to be considered [44, 45, 48, 50] in order to ensure that upper states are in partial local Saha equilibrium with the ion and the population of the lower states are unaffected by the truncation. Collisional–radiative models require cross-section data and transition probabilities of the corresponding processes which are still incomplete so that semi-empirical expressions have to be applied. In order to reduce the number of states and hence the computational effort, the states are usually lumped into effective levels and the system of rate equations is solved assuming quasi-steady-state (QSS) conditions. This assumption is justified by the much shorter relaxation times of the excited states in comparison with the relaxation time of the ground state of atoms and ions. In the collisional-radiative model used in the present work, the ground state atomic density, the electron temperature and density obtained with fully nonequilibrium arc model are set as input parameters. A cut-off approach combining

analytical and numerical techniques is applied as proposed in [49] that allow reducing significantly the number of levels that must be taken into account. In the present study, a QSS-calculation of the atomic state distribution [51] is carried out taking into account 31 individual or effective excited levels. About 1100 processes are taken into account to describe excitation/deexcitation, emission, ionization and recombination in electron-atom collisions but not of atom-atom collisions. According to the results reported in [52], the latter have been found to be of minor importance in a free-burning arc in argon at atmospheric pressure. The plasma is assumed optically thin for all radiative transitions except for resonance radiation which is treated as locally absorbed. The latter has been approved by means of a collisional-radiative model accounting for transport of resonance radiation [53].

Results and Discussion

The arc arrangement shown in Fig. 1 follows the description of the experimental setup given in [24] which is similar to the configuration studied in [4–7] and in other works on wall-stabilized arcs. Unfortunately, the operating conditions in the various experiments have not been identical with respect to arc current, inter-electrode distance, shape of the cathode, and gas flow rate or some parameters even have not been reported. The conditions in the arc model are chosen close to reported in experiments.

The Cylindrical Column of the Wall-Stabilized Arc Plasma

At a sufficient distance from the electrode regions, axial gradients are small and the plasma properties can be considered as functions of the radial position only. Line-out through the middle of the constrictor tube and perpendicular to the arc axis (dash line (1) in Fig. 1) is used to present the radial course of the plasma properties.

Figure 2 presents the radial distribution of electron and heavy particle temperatures obtained with the nonequilibrium arc plasma model for arc currents of 35, 60 and 150 A.

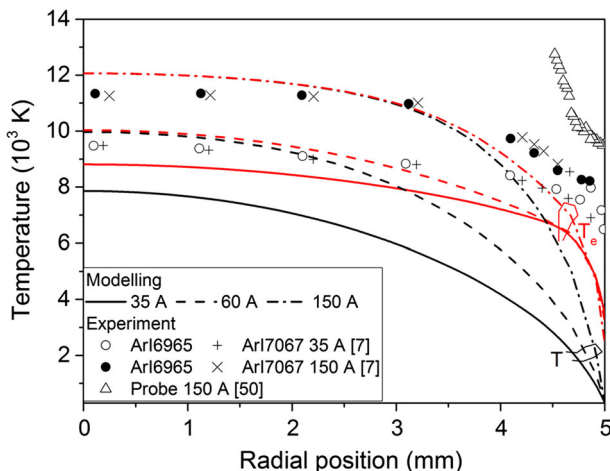


Fig. 2 Temperature profiles from modelling (*lines*), line [7] and probe [54] measurements (*symbols*)

Experimental values at the same current levels and attributed to the electron temperature are also plotted. Notice that the experimental results in [7] are obtained after transformation of experimental findings using the Boltzmann distribution and equilibrium properties. The arc model is run with gas flow rate 0.135 g s^{-1} , 10 mm distance between the end of the constrictor tube and the anode. Similar gas flow rate is reported for the experiments in [7]. Information concerning the other conditions is not available. Therefore, the comparison especially close to the wall, i.e. radial position 5 mm, is rather qualitative. Nevertheless, the difference between the calculated electron temperature and the values reported from line measurements [7] is in the most part within 10^3 K . The values obtained in probe measurements [54] close to the tube wall exceed both the calculated and the experimental results in [7]. A common trend is that the electron temperature is several thousands kelvin higher than the temperature of heavy particles which approaches the temperature of the surface at the wall. However, the experimental values at arc current of 35 A exceed the predicted values over the entire length, while at 150 A this appears in the half part of the distance towards the wall. The modelling results further show strong departure from thermal equilibrium along the entire distance at 35 A and in the half part of the distance towards the wall at 150 A. Hence, the values derived in [7] assuming LTE conditions at current levels and regions where departure from equilibrium occurs are systematically higher than the results of the fully nonequilibrium model. In the central part of the arc column, the experimental values are quite closer to but slightly lower than the calculated ones at 150 A (dash-dot line). The results of probe measurements [54] at 150 A, however, should be insensitive with respect to the nonequilibrium conditions since the interpretation of the experimental data does not require any assumption about the thermodynamic state of the plasma. Due to the incomplete information about the operating conditions in [54], it is very likely that the reason for higher electron temperature values close to the constrictor wall is in the conditions. Modelling results for arc current of 60 A are also presented in Fig. 2 to show that, this current value indicates the separation of the regime of thermal nonequilibrium over the entire radius from the regime of thermal equilibrium in the central part of the arc column and nonequilibrium towards the wall.

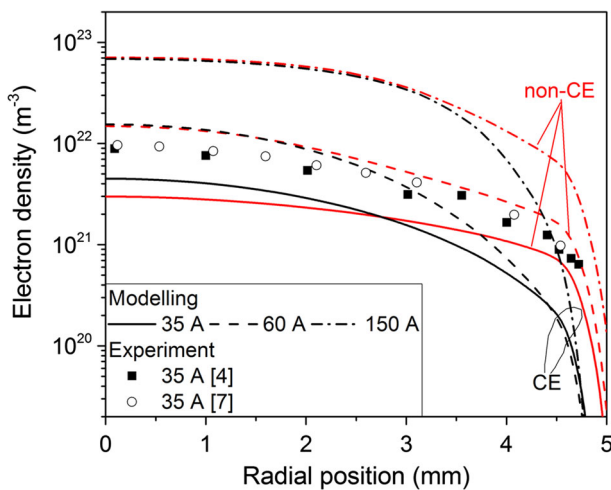


Fig. 3 Radial profiles of electron density from modelling (*non-CE lines*) and measurements (*symbols*). Electron density from ionization equilibrium (*CE-lines*)

Figure 3 shows the radial distribution of the electron density obtained with the fully nonequilibrium model arc model (non-CE lines) at the same current levels as in Fig. 2 (35, 60 and 150 A), the electron density obtained assuming chemical (ionization) equilibrium at local values of electron and heavy particle temperature from the arc model (CE-lines), and electron density from measured data [4, 7] evaluated under LTE assumption at arc current of 35 A. At arc current of 60 A, the calculated non-CE electron density is slightly lower than the CE-value in the central part of the plasma column but exceeds the CE-density by far towards the wall. The departure from chemical (ionization) equilibrium is appreciable under conditions of thermal nonequilibrium along the whole radius (35 A). At arc current of 150 A, the non-CE density exceeds the CE-density over the entire distance but the difference becomes more and more pronounced beyond the radial position of 3 mm. At this position, the electron and heavy particle temperatures begin to separate (Fig. 2) so that the chemical (ionization) nonequilibrium is intensified by the thermal nonequilibrium.

Figure 4 presents the atomic state distribution function in logarithmic scale in terms of the ratio of the density of atomic states divided by the corresponding statistical weight and the density of the ground state for a series of radial positions along the line-out (1) in Fig. 1 for arc currents of 35 A (a) and 150 A (b). The solid lines present the atomic state distribution obtained from the two-temperature Saha–Boltzmann equation assuming ionization equilibrium (2T-CE) and the dash lines present the values from the QSS-calculation. The low-current case in Fig. 4a represents the most severe nonequilibrium conditions as discussed in relation to Figs. 2 and 3. Although the excitation is relatively weak, the excitation nonequilibrium is clearly pronounced. Close to the axis of the plasma column of the wall-stabilized arc (radial position $r = 0$) till the half radius of the plasma column, the 2T-CE values overpredict the QSS-values due to the higher electron density obtained under conditions of chemical equilibrium. Towards the wall, the excitation nonequilibrium occurs in overpopulation of the levels compared with the equilibrium value since the departure of the non-CE electron density from the CE-value becomes progressively more pronounced. In the high-current case (Fig. 4b), the excitation nonequilibrium is less pronounced in the inner region of the plasma column where the plasma state is close to LTE. In contrast, thermal and chemical nonequilibria in the outer region intensify the overpopulation of the excited atomic levels and lead to excitation nonequilibrium. Further effect of chemical nonequilibrium is the overpopulation of the ground state with respect to its CE-value which is more pronounced in the inner part of the plasma column (barely visible on the graphs). This effect has been reported for low-current and wall-stabilized arcs in noble gases [4, 8, 12]. Argon atoms vanishing in the central part are renewed by net inward diffusive transport. Therefore, the excitation temperature of the excited states is determined from the slope of the atomic state distribution function (Fig. 4) excluding the ground state. It is found to equal the electron temperature along the radius except in the immediate vicinity of the wall where the electron density is sharply reduced.

Densities of $4s$ and $4p$ levels of Ar for arc current of 35 A are presented in Fig. 5. Lines of ArI at 696.5 and 706.7 nm have been studied in [4, 7]. These lines originate from states of the $4p$ level and terminate at the same state of the $4s$ level. The results correspond to (1) modelling predictions in the present work which are based on Saha–Boltzmann distribution and two-temperature composition under chemical equilibrium (CE) applying temperatures of heavy particles and electrons from the fully nonequilibrium arc model, (2) collisional-radiative QSS-model (non-CE) applying temperatures of heavy particles and electrons and electron density from the fully nonequilibrium arc model, (3) LTE evaluation reported in [7], (4) experimental data reported in [4, 7], and (5) collisional–radiative model reported in [7]. Quantitative comparison is rather difficult since experimental and modelling results are

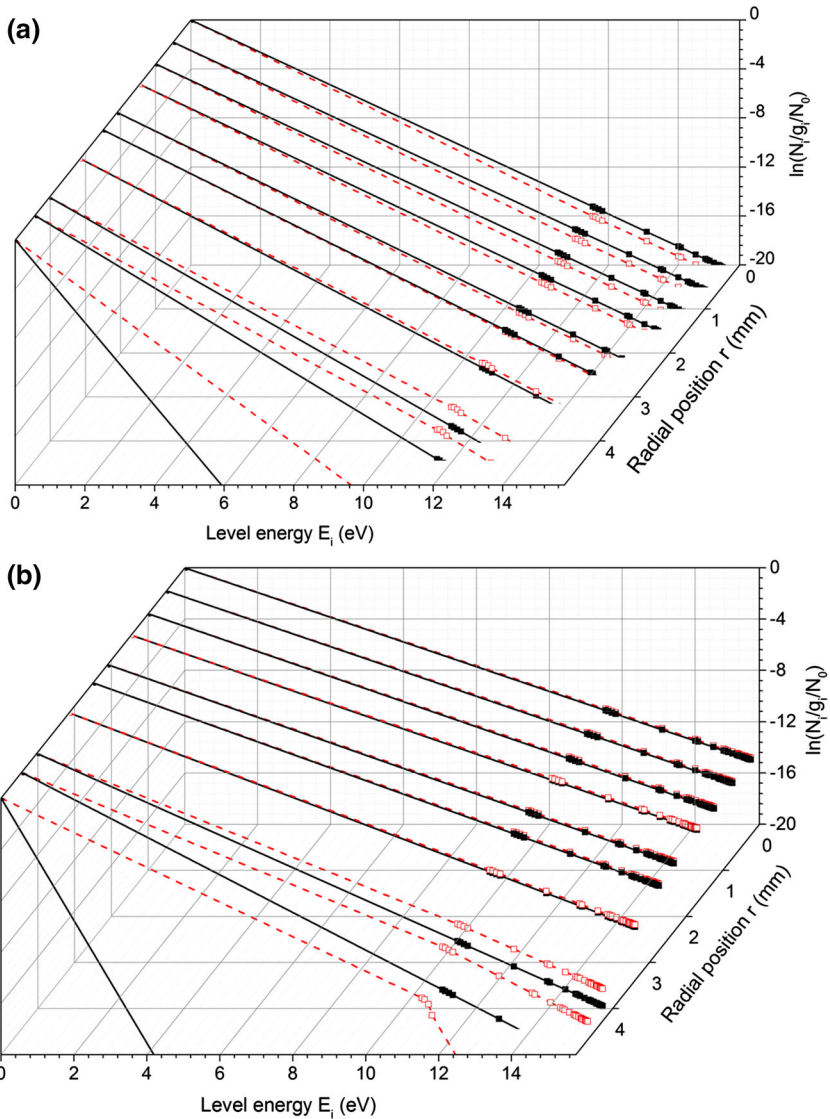
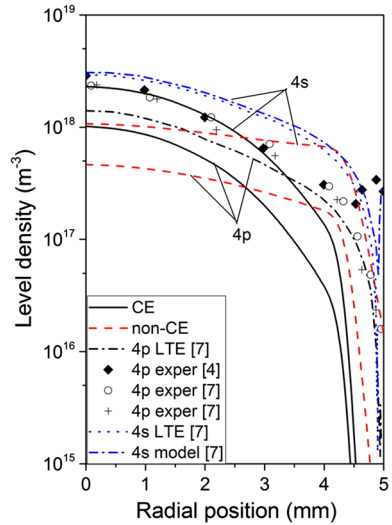


Fig. 4 Atomic state distribution for various radial positions along line-out (1) (Fig. 1) from two-temperature composition and assumption of ionization equilibrium (*solid lines and solid symbols*) and QSS collisional-radiative model (*dash lines and open symbols*). Arc current **a** 35 A, and **b** 150 A

derived at somewhat different conditions, e.g. assuming thermal equilibrium and hot walls in [4, 7] even at low currents. A detailed reproduction of the conditions in [4, 7], even if all conditions were known, is out of the scope of the present work. Here, the focus is on the evidence of chemical and excitation nonequilibrium. The electron temperature from the nonequilibrium arc model is lower than the temperature values in [4, 7] throughout the arc radius which explains in general the lower density (within a factor of 2–3) of 4s and 4p levels obtained in the present study. Overpopulation in the case of ionization

Fig. 5 Number density of $4s$ and $4p$ levels of Ar atoms from experiments reported in [4, 7] and modelling predictions reported in [7] and the present work (CE, non-CE). Arc current 35 A



equilibrium (CE) with respect to the nonequilibrium values (non-CE) can be seen in the central part of the arc for both $4s$ and $4p$ levels whereas in [7] the equilibrium $4s$ density values are underpredicted with respect to the those from the collisional-radiative model. Since in [7] the plasma is considered as optically thick only in the vicinity of the wall, a secondary peak in the $4s$ level density occurs. The latter is explained as a result of inadequate electron-atom collisional exchange, radiative transitions originating from upper levels and trapping of resonance radiation [7]. The $4p$ level population reported in [4] indicates a secondary peak towards the wall which is not confirmed by the results in [7]. The results in [4] are within a factor of 2 higher than those in [7]. The $4s$ and $4p$ level densities obtained in the present study (CE and non-CE) are consistent with the behaviour of the electron density (Fig. 3) which has the main impact on the collisional excitation.

The Anode Region

The arc region between the end of the constrictor tube and the anode is influenced by effects resulting from the electric current and fluid dynamics. In a large number of publications [27–30], this region has been simulated separately from the rest of the arc. The main assumption in these works is that in a fully developed arc column (see e.g. [27, 55]) the thermal and flow fields are independent of each other, which means that the velocity field is related only to the mass flow rate. Therefore, boundary conditions are set at the line-out (2) in Fig. 1 based on the solutions of arc plasma flow [27] for the temperature and velocity profiles, the Saha equation with assumption of LTE for the electron density, electric current density profile from the free-arc simulations [56]. Modelling of the entire arc is advantageous since it overcomes the setting of boundary conditions which are not completely consistent. Changes in the mass flow rate of the gas affects the cathode region of the arc. The attachment area on the cathode extends with decreasing mass flow rate. As a result, the current density at the cathode tip is lower which in turn has impact on the cathode jet flow, the temperature in the arc core and the arc voltage. The plasma conditions in the long arc column do not change a lot so that the assumption of a fully developed arc column and scaling of the mass flow rate with scaling the flow velocity at the end of the

constrictor tube (line-out (2) in Fig. 1) can be considered as reasonable. Moreover, the modelling of the anode region separated from the constrictor tube avoids the circumstances related to the pressure drop along the tube which is caused by the hydraulic resistance (proportional to the ratio tube length over tube diameter). Under experimental conditions, the pressure gradient is reduced by separating the segments building the constrictor channel by a distance of 1 mm [24]. To complicate the geometry according to the experimental setup in [24] would reduce the pressure drop however it is out of the scope of the present work.

Figure 6 shows the distribution of electron and heavy particle temperatures in the region between the end of the constrictor tube and the anode which are obtained from the solution of a) the entire arc and b) the region below the line-out (2) in Fig. 1 as it has been done in [27–30]. The latter simulation applies boundary conditions on the line-out (2) placed 1 mm above the end of the constrictor tube in order to avoid effects caused by the tube edge. Normalized arrow indicators represent the direction of the gas flow. The full arc model is run with a mass flow rate of 0.135 g s^{-1} and an arc current of 200 A. The distance between

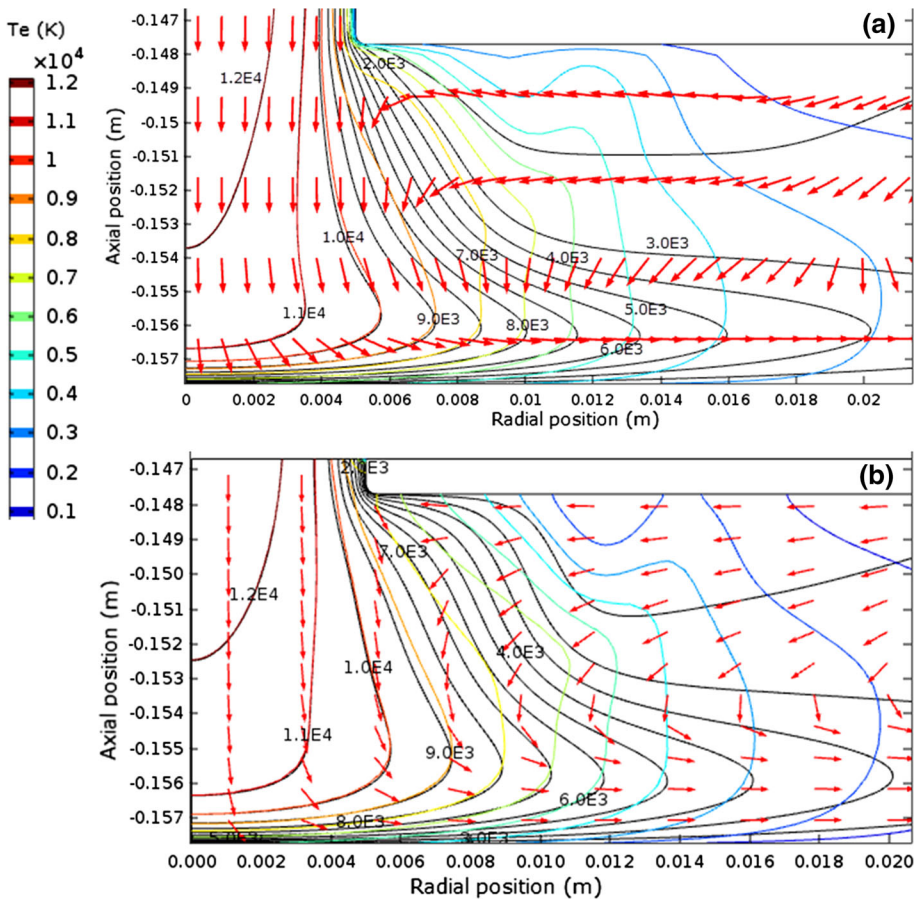


Fig. 6 Temperatures in kelvin of heavy particles (*black contours*) and electrons (*coloured contours*) and flow direction (*arrows*) obtained from **a** the full arc model, **b** the model of the region between the end of the constrictor tube and the anode. Mass flow rate 0.135 g s^{-1} , arc current 200 A

the end of the constrictor tube and the anode is 10 mm. The radial length of the anode is 40 mm to provide realistic boundary conditions at the open boundary.

The results show qualitative and quantitative similarities of the solutions, although the hot arc region enclosed by the line of 12,000 K is slightly longer and the departure from thermal equilibrium occurring below 10,000 K is a bit more pronounced in the full arc model. The hot gas flow impinges on the anode surface and is directed towards the open boundary, while cold gas flows close to the end of the constrictor tube towards the arc. The arc is dominated by the cathode jet and exhibits a bell-shape which is typical for diffuse arc attachment on the anode [24].

The anode-part model of the arc is further applied for a mass flow rate reduced by a factor of 0.3. The result is presented in Fig. 7. It is evident that the hot arc region is shortened, the 12,000 K line is almost on the height of the edge of the constrictor tube. The cathode jet does not dominate the arc flow. Instead, an anode jet is built which collides with the cathode jet approximately 1 mm below the edge of the constrictor tube. The hot gas flows towards the open boundary along the bottom edge of the constrictor tube, while cold gas flows along the anode surface towards the arc. The arc attachment on the anode becomes constricted. The result confirms the experimental findings in [57] and the modelling predictions in [55]. The region of thermal nonequilibrium in front of the anode is extended in axial direction in comparison to the diffuse arc attachment (Fig. 6). An overview of the processes and conditions in the anode region is given in [58]. It underlines the role of macroscopic flows for the formation of constricted arc attachment.

The axial distribution of temperatures of heavy particles and electrons is presented in Fig. 8a for diffuse and constricted arc attachment. While in the case of diffuse attachment thermal nonequilibrium occurs at a distance of about 0.5 mm from the anode, the region of thermal nonequilibrium spreads out over a length of about 3 mm in the case of constricted arc attachment. Deviation from ionization equilibrium occurs throughout the arc axis (Fig. 8b). However, the behaviour is different in the two cases. In the case of diffuse attachment, the nonequilibrium electron density (non-CE) exceeds the equilibrium one

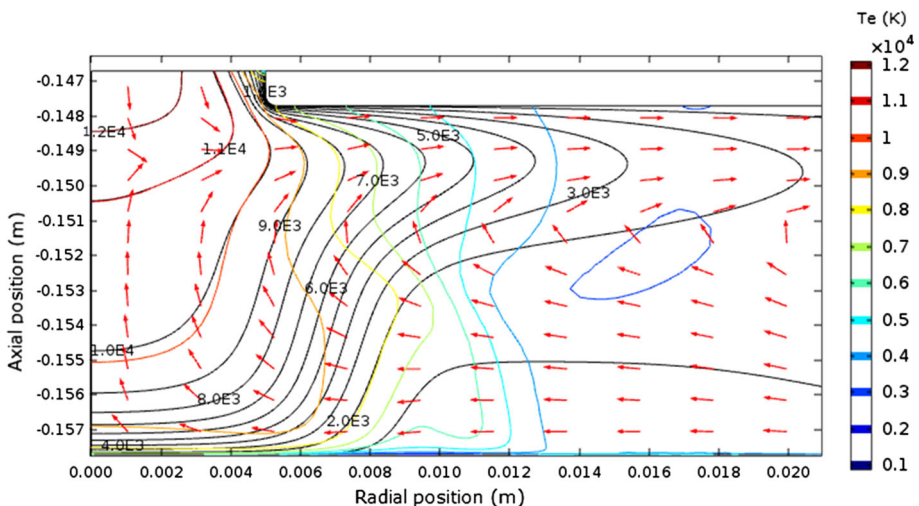


Fig. 7 Temperatures in kelvin of heavy particles (*black contours*) and electrons (*coloured contours*) and flow direction (*arrows*) obtained from the model of the region between the end of the constrictor tube and the anode. Mass flow rate 0.04 g s^{-1} , arc current 200 A

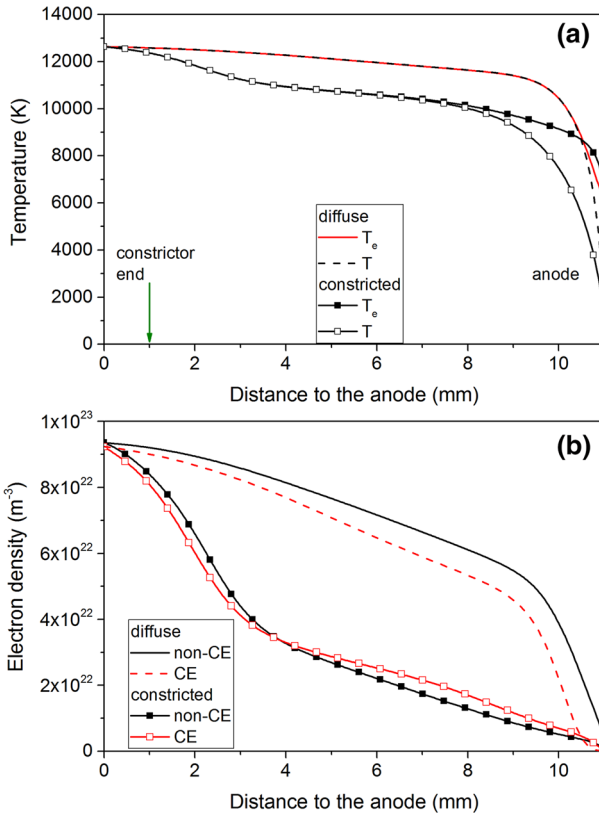


Fig. 8 Temperatures of heavy particles and electrons along the arc axis (a) and electron density (b) in the case of diffuse and constricted arc attachment on the anode. Arc current 200 A. Electron density is obtained from the fully nonequilibrium arc model (*non-CE*) and two-temperature Saha equation (*CE*)

(*CE*) over the entire length. In the case of constricted arc attachment, this effect occurs in the first third of the length. The nonequilibrium electron density (*non-CE*) is lower than the equilibrium one (*CE*) over the remaining length. The turning point is close to the axial position where the cathode and the anode jets meet each other (Fig. 7). The position of flow stagnation for constricted arc attachment is indicated in Fig. 9 by means of a dash line perpendicular to the arc axis. Notice that the positive direction is away from the anode so that the anode jet velocity is positive whereas that of the cathode jet is negative. At the same position, the modulus of the axial electric field exhibits a local minimum in the constricted arc. Further difference between the diffuse and constricted mode is the position of field reversal in the vicinity of the anode. It is closer to the anode in the constricted mode. Field reversal is observed in both diffuse and constricted mode under the conditions considered. Correspondingly, negative anode fall in the electric potential is observed in both modes. However, for diffuse arc attachment it is about 3 V, while for constricted arc attachment its value is slightly below 1 V. The negative anode fall occurs due to strong diffusive fluxes in the anode region and is therefore closely related to the nonequilibrium effects there.

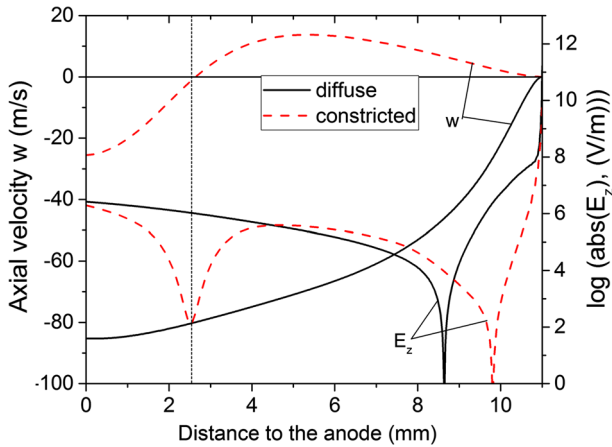


Fig. 9 Axial flow velocity (w) and modulus of electric field (E_z) along the arc axis for diffuse and constricted arc attachment on the anode. Arc current 200 A

The electric field reversal in the vicinity of the anode corresponds to a negative Joule heating term in the equation of total energy balance. This effect has been qualitatively assigned as a formation of an electric generator [59, 60], which in the case of a diffuse arc attachment is sustained by the thermal power delivered by the plasma jet. However, for a constricted arc attachment, the origin of the power supply remained unclear so far [58]. The equations of energy conservation for electrons and heavy particles can be summed up and the result can be rewritten as a balance with respect to the Joule heating. Then, the terms representing a gain or a loss of energy due to (1) inelastic collisions (ionization and recombination) and radiation, (2) the convective transport associated with the fluid flow, and (3) the divergence of energy fluxes of electrons and heavy particles accounting for thermal conduction, transport of enthalpy by diffusion fluxes, and thermal diffusion must compensate the Joule heating term. These terms are plotted in Fig. 10 for a diffuse and a constricted arc attachment on the anode. Shown is the axial distance of approximately 3 mm in front of the anode, where the electric field reversal occurs in both cases (Fig. 9). The following conclusions can be drawn. The power release due to inelastic collisions and radiation is the smallest contribution beyond the point of reversal both for a diffusive and a constricted arc attachment, although its role in the case of a diffuse arc attachment is comparable with that of the convective heat transport. The reason is the higher electron density (Fig. 8) in the diffuse mode. The convective transport term and the divergence of energy flux are of opposite signs in both cases up to a distance of approximately 0.25 mm from the anode. This correlates with the direction of the associated gas flow and the profile steepness of the temperatures and the electron density (Fig. 8). In the proximity of the anode, the divergence of energy flux is the term, which provides the balance with the Joule heating term.

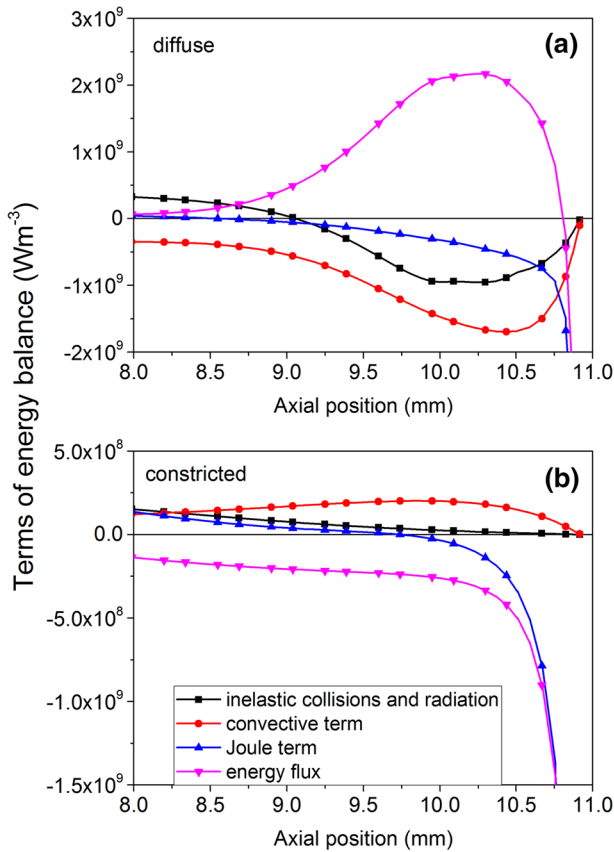


Fig. 10 Terms of the total energy balance along the arc axis for **a** diffuse and **b** constricted arc attachment on the anode. Arc current 200 A

Concluding Remarks

The present work is concerned with the nonequilibrium behaviour of a wall-confined arc and its near-anode region in argon at atmospheric pressure by means of an advanced fully nonequilibrium model. Deviations from chemical (ionization) equilibrium are evident in the plasma column and the anode region.

In the fully developed arc column at low arc current (35 A), the deviation is appreciable under conditions of thermal nonequilibrium occurring throughout the plasma radius. Current value of 60 A indicates the separation of the regime of thermal nonequilibrium over the entire radius from the regime of thermal equilibrium in the central part of the arc column and nonequilibrium towards the wall. In this case, the calculated nonequilibrium electron density is slightly lower than the value obtained under assumption of chemical equilibrium in the central part of the plasma column but exceeds the latter by far towards the wall. At higher arc current (150 A), the nonequilibrium electron density exceeds the equilibrium one over the entire radial distance but the difference becomes strongly pronounced beyond the radial position of 3 mm, where the electron and heavy particle

temperatures begin to separate so that the chemical (ionization) nonequilibrium is intensified by the thermal nonequilibrium.

In the anode region even for an arc current of 200 A, deviation from ionization equilibrium occurs throughout the arc axis. Two modes of arc attachment on the anode are demonstrated depending on the mass flow rate, for which the behaviour is different. For diffuse attachment, the nonequilibrium electron density exceeds the equilibrium one over the entire distance to the anode. In the case of constricted arc attachment, this effect occurs in the first third of the length. The nonequilibrium electron density is lower than the equilibrium one over the remaining length. The different behaviour is attributed to the vanishing role of the cathode jet and the occurrence of anode jet. The changing flow conditions are related to diffusive transport in the anode region and the position of the reversal of electric field and the magnitude of negative anode fall.

The chemical nonequilibrium results in nonequilibrium of the atomic state distribution since the excitation of atomic states is closely related to electron density.

The results of the present work are presented along with published experimental and modelling data to show the qualitative and quantitative agreement but also the differences observed.

Acknowledgements This work was supported by the DFG (German Science Foundation) under Grant UH106/11-1. The author thanks Professor Jürgen Mentel and Professor Jürgen Uhlenbusch for valuable discussions. The author is grateful to Professor Maher Boulos and Professor Pierre Fauchais for the kind invitation to contribute to the special issue dedicated to honor the memory of Professor Emil Pfender.

References

1. Maecker H (1960) Messung und Auswertung von Bogencharakteristiken (Ar, N₂). *Z Phys* 158:392–404
2. Emmons HW, Land RI (1962) Poiseuille plasma experiment. *Phys Fluids* 5(12):1489–1500
3. Uhlenbusch J (1964) Berechnung der Materialfunktionen eines Stickstoff- und Argonplasmas aus gemessenen Bogenwerten. *Z Phys* 179:347–366
4. Bott JF (1966) Spectroscopic measurement of temperatures in an argon plasma arc. *Phys Fluids* 9:1540–1547
5. Kruger CH (1970) Nonequilibrium in confined-arc plasmas. *Phys Fluids* 13:1737–1746
6. Giannaris RJ, Incropera FP (1971) Nonequilibrium effects in atmospheric argon arc plasma. *J Quant Spectrosc Radiat Transf* 11:291–307
7. Giannaris RJ, Incropera FP (1973) Radiative and collisional effects in cylindrically confined plasma—I. Optically thin considerations. *J Quant Spectrosc Radiat Transf* 13:167–181
8. Uhlenbusch J (1974) Non-equilibrium effects in arc discharges. In: McGowan JW, John PK (eds) *Gaseous electronics. Some applications*. North-Holland, Amsterdam, pp 101–132
9. Bacri J, Gomes AM, Benzaid S (1976) Etude des écarts à l'ETL dans un arc d'argon ($P = 760$ Torr). *J Phys D Appl Phys* 9:1743–1755
10. Musielok J (1977) Non-equilibrium effects in He–Ar–H arc plasma. *Beitr Plasmaphys* 17:135–143
11. Gleizes A (1981) Role of recombination, ionization, diffusion and convection in a decaying argon plasma. *Physica* 111C:386–396
12. Timmermans CJ, Rosado RJ, Schram DC (1985) An investigation of non-equilibrium effects in thermal argon plasmas. *Z Naturforschung* 40a:810–825
13. Cram LE, Poladian L, Roumellotis G (1988) Departures from equilibrium in a free-burning argon arc. *J Phys D Appl Phys* 21:418–425
14. Farmer AJD, Haddad GN (1988) Rayleigh scattering measurements in a free-burning argon arc. *J Phys D Appl Phys* 21:426–431
15. Chang CH, Ramshaw JD (1994) Numerical simulation of nonequilibrium effects in an argon plasma jet. *Phys Plasmas* 1(11):3698–3708
16. Pokrzywka B, Musioł K, Pellerin S, Pawelec E, Chapelle J (1996) Spectroscopic investigation of the equilibrium state in the electric arc cathode region. *J Phys D Appl Phys* 29:2644–2649

17. Kühn G, Kock M (2006) A spatially resolved relaxation method for pLTE plasma diagnostics in free-burning arcs. *J Phys D Appl Phys* 39:2401–2414
18. Kühn G, Kock M (2007) Nonequilibrium phenomena and determination of plasma parameters in the hot core of the cathode region in free-burning arc discharges. *Phys Rev E* 75:016406
19. Bergner A, Scharf FH, Kühn G, Ruhrmann C, Hoebing T, Awakowicz Mentel J (2014) Simulation of the hot core mode of arc attachment at a thoriated tungsten cathode by an emitter spot model. *Plasma Sources Sci Technol* 23:054005
20. Baeva M (2016) Thermal and chemical nonequilibrium effects in free-burning arcs. *Plasma Chem Plasma Process* 36:151–167
21. Cram LE (1985) Synthesis of emission line profiles from free-burning arcs. *J Quant Spectrosc Radiat Transf* 34(4):353–357
22. Haddad GN, Farmer AJD (1984) Temperature determinations in a free-burning arc: I. Experimental techniques and results in argon. *J Phys D Appl Phys* 17:1189–1196
23. Kovitya P, Lowke JJ (1985) Two-dimensional analysis of free burning arcs in argon. *J Phys D Appl Phys* 18:53–70
24. Pfender E (1980) Energy transport in thermal plasmas. *Pure Appl Chem* 52:1773–1800
25. Benilov MS (1999) Modeling of a nonequilibrium cylindrical column of a low-current arc discharge. *IEEE Trans Plasma Sci* 27(5):1458–1463
26. Dinulescu HA, Pfender E (1980) Analysis of the anode boundary layer of high intensity arcs. *J Appl Phys* 51(6):3149–3157
27. Chen DM, Pfender E (1981) Two-temperature modelling of the anode contraction region of high-intensity arcs. *IEEE Trans Plasma Sci* 9(4):265–274
28. Wilhelm H, Wimmer W, Pfender E (1985) Modeling of the transport phenomena in the anode region of high current arc. *Numer Heat Transf* 8:731–749
29. Jenista J, Heberlein JVR, Pfender E (1997) Numerical model of the anode region of high-current electric arcs. *IEEE Trans Plasma Sci* 25(5):883–890
30. Park J, Heberlein J, Pfender E, Candler G, Chang CH (2008) Two-dimensional numerical modeling of direct-current electric arcs in nonequilibrium. *Plasma Chem Plasma Process* 28:213–231
31. Baeva M, Benilov MS, Almeida NA, Uhrlandt D (2016) Novel non-equilibrium modelling of a DC electric arc in argon. *J Phys D Appl Phys* 49:245205
32. Zhdanov VM (2002) Transport phenomena in multicomponent plasma. Taylor and francis, London
33. Ramshaw JD (1990) Self-consistent effective binary diffusion in multicomponent gas mixtures. *J Non-Equilib Thermodyn* 15(3):295–300
34. Ramshaw JD, Chang CH (1993) Ambipolar diffusion in two-temperature multicomponent plasmas. *Plasma Chem Plasma Process* 13(3):489–498
35. Hoffert MI, Lien H (1967) Quasi-one-dimensional, nonequilibrium gas dynamics of partially ionized two-temperature argon. *Phys Fluids* 10(8):1769–1777
36. Bond JW, Watson KM, Welch JA (1965) Atomic theory of gas dynamics. Addison-Wesley, Reading
37. Byron S, Stabler RC, Bortz PI (1962) Electron-ion recombination by collisional and radiative processes. *Phys Rev Lett* 8(9):376–379
38. Freton P, Gonzalez JJ, Ranarijaona Z, Mougenot J (2012) Energy equation formulations for two-temperature modelling of “thermal plasmas”. *J Phys D Appl Phys* 45:465206
39. Evans DL, Tankin RS (1967) Measurement of emission and absorption of radiation by an argon plasma. *Phys Fluids* 10(6):1137–1144
40. Menart J, Malik S (2002) Net emission coefficients for argon-iron thermal plasmas. *J Phys D Appl Phys* 35:867–874
41. Beulens JJ, Milojevic D, Schram DC, Vallinga M (1991) A two-dimensional nonequilibrium model of cascaded arc plasma flows. *Phys Fluids* 3:2548–2557
42. Rat V, Murphy AB, Aubreton J, Elchinger MF, Fauchais P (2008) Treatment of non-equilibrium phenomena in thermal plasma flows. *J Phys D Appl Phys* 41:183001
43. Benilov MS, Almeida NA, Baeva M, Cunha MD, Benilova LG, Uhrlandt D (2016) Account of near-cathode sheath in numerical models of high-pressure arc discharges. *J Phys D Appl Phys* 49:215201
44. Katsonis K (1976) Etude statistique et cinétique des plasmas d’argon en dehors de l’équilibre thermodynamique local. These Univ, Paris Sud, Centre d’Orsey
45. Bates DR, Kingston AE, McWhirter RWP (1962) Recombination between electrons and atomic ions. I. Optically thin plasmas. *Proc R Soc A* 267:297–312
46. Bacri J, Gomes AM (1978) Influence of atom-atom collisions on thermal equilibrium in argon arc discharges at atmospheric pressure. *J Phys D Appl Phys* 11:2185–2197
47. Van der Sijde B, Van der Mullen JJAM, Schram DC (1984) Collisional radiative models in plasmas. *Beitr Plasmaphys* 24:447–473

48. Vlček J (1989) A collisional-radiative model applicable to argon discharges over a wide range of conditions. I: formulation and basic data. *J Phys D Appl Phys* 22:623–631
49. Benoy DA, Van der Mullen JAM, Van der Sijde B, Schram DC (1991) A novel collisional radiative model with a numerical bottom and an analytical top. *J Quant Spectrosc Radiat Transf* 46(3):195–210
50. Bogaerts A, Gijbels R, Vlček J (1998) Collisional–radiative model for an argon glow discharge. *J Appl Phys* 84(1):121–136
51. Hartgers A, van Dijk J, Jonkers J, van der Mullen JAM (2001) CRModel: a general collisional radiative modelling code. *Comput Phys Commun* 135:199–218
52. Baeva M (2016) Thermal and chemical nonequilibrium effects in free-burning arcs. *Plasma Chem Plasma Process* 36:151–167
53. Golubovskii Yu, Kalanov D, Gortschakow S, Baeva M, Uhrlandt D (2016) Excited atoms in the free-burning Ar arc: treatment of the resonance radiation. *J Phys D Appl Phys* 49:475202
54. Leveroni E, Pfender E (1989) Electric probe diagnostics in thermal plasmas: double probe theory and experimental results. *Rev Sci Instrum* 60(12):3744–3749
55. Amakawa T, Jenista J, Heberlein J, Pfender E (1998) Anode-boundary-layer behaviour in a transferred, high-intensity arc. *J Phys D Appl Phys* 31:2826–2834
56. Hsu KC, Pfender E (1983) Two-temperature modelling of the free-burning, high-intensity arc. *J Appl Phys* 54(8):4359–4366
57. Hartmann RV, Heberlein JV (2001) Quantitative investigations on arc-anode attachments transferred arcs. *J Phys D Appl Phys* 34:2972–2978
58. Heberlein J, Mentel J, Pfender E (2010) The anode region of electric arcs: a survey. *J Phys D Appl Phys* 43(2):023001
59. Mentel J, Heberlein J (2010) The anode region of low current arcs in high intensity discharge lamps. *J Phys D Appl Phys* 43:023002
60. Hoebing T, Bergner A, Hermanns P, Mentel J, Awakowicz P (2016) The anodic emitter effect and its inversion demonstrated by temperature measurements at doped and undoped tungsten electrodes. *J Phys D Appl Phys* 49:155504